Journal of
Materials Chemistry B

Accepted Manuscript

This article can be cited before page numbers have been issued, to do this please use: Q. Tang, W. Si, C. Huang, K. Ding, W. Huang, P. Chen, Q. Zhang and X. Dong, *J. Mater. Chem. B*, 2017, DOI: 10.1039/C6TB02979E.

ROYAL SOCIETY OF CHEMISTRY

rsc.li/materials-b

View Article Online
DOI: 10.1039/C6TB02979E

Journal Name

ARTICLE

Aza-Bodipy Photosensitizer for Photoacoustic and Photothermal Imaging Guided Dual Modal Cancer Phototherapy†

Received 00th January 20xx,
Accepted 00th January 20xx

DOI: 10.1039/x0xx00000x

www.rsc.org/

Qianyun Tang,[a] Weili Si,[a] Chuhan Huang,[a] Kaikai Ding,[a] Wei Huang,[a] Peng Chen,*[b] Qi Zhang,*[c] Xiaochen Dong*[a]

Developing biocompatible, near infrared absorbing, and multi-functional photosensizers is critical for effective cancer phototherapy. In this contribution, a BF_2 chelate of [4-iodo-5-(4-bromophenyl)-3-(4-methoxyphenyl)-1H-pyrrol-2-yl][4-iodo- 5-(4-bromophenyl)-3-(4- methoxyphenyl)pyrrol-2-ylidene]amine (IABDP) with high singlet oxygen generation efficiency (~92%) has been designed and synthesized. The soluble and near infrared adsorbing nanoparticles (NPs) can be simply obtained from self-assembly of IABDP molecules, which has a high photothermal conversion efficiency (~37.9%). Under irradiation of a broadband Xenon lamp, IABBDP NPs are able to serve as the common photosensitizer for photothermal imaging (PTI) and photoacoustic imaging (PAI) guided simultaneous photodynamic therapy (PDT) and photothermal therapy (PTT). Comparing to the usual combined strategies that require two distinct photosensitizers and two excitation sources, IABBDP NP based approach is much simplified, hence more convenient, reliable, and cost effective. Both *in vitro* and *in vivo* studies confirm the good biosafety and prominent anti-tumor phototoxicity of IABDP NPs. Finally, we demonstrate that the imaging guided synergistic dual modal phototherapy enabled by IABDP NPs can essentially inhibit tumor growth (87.2% inhibition) in mice without causing appreciable side-effects, testifying the great potential of this multi-functional organic photosensizer for clinical use.

Introduction

Phototherapy for cancers, including photodynamic therapy (PDT) and photothermal therapy (PTT), has attracted tremendous research effort because of some unique advantages over the conventional treatments, such as low toxicity, high selectivity, minimal invasiveness, no issue of drug tolerance.[1] PDT relies on the photosensitizer to generate reactive oxygen species (ROS, such as singlet oxygen $^1O_2$, superoxide anion radical O^{2-}, and hydroxyl radical $^{\cdot}OH$) under irradiation, which, in turn, destroy tumor cells and tumor blood vessels.[2] However, the efficacy of PDT is severely compromised by the inherent hypoxic microenvironment in tumor tissues and the poor light penetration depth because most PDT photosensitizers are activated by ultraviolet or visible light.[3] PTT is a therapeutic strategy in which photon energy is converted into heat to burn tumor cells. Most current photosensitizers (or photothermal agents) for PTT absorb light in near-infrared (NIR, 700-1100 nm) region, which is known as the transparent window for deep tissue penetration.[4] However, the remnant cells may swiftly develop heat resisting property, leading to cancer relapse and metastasis.[5] The efficacy of phototherapy should be greatly enhanced by synergistic combination of PDT and PTT. But the key towards this ambition is to devise a biocompatible photosensitizer which can produce ROS and heat simultaneously upon NIR irradiation. Moreover, mild hyperthermia induced by PTT can improve vascular perfusion whereby relieving the hypoxic condition in tumor and enhancing extravasation of therapeutic nanoparticles into the tumor interstitium.[6]

Recently, efforts have been made to develop imaging-guided cancer therapy in order to improve the effectiveness and reduce the side-effects through precisely locating tumor sites, optimizing treatment time, and monitoring treatment progress.[7] Photothermal imaging (PTI) is often applied in conjunction with PTT.[8] Although offering good temperature sensitivity and possibility of real-time monitoring, PTI however provides poor spatial resolution.[9] Photoacoustic imaging (PAI) based on the thermal wave generated by the photosensitizer may be employed, which is a new non-ionizing and non-invasive imaging modality with high optical contrast, good penetration depth and high spatial resolution.[10]

Some inorganic nanomaterials (e.g., gold,[11] carbon,[12] metal oxide,[4, 13] or metal sulfide nanoparticles[14]) have been utilized to realize imaging-guided synergistic phototherapy. But the practice use of these methods is largely hindered by

[a] Key Laboratory of Flexible Electronics (KLOFE) and Institute of Advanced Materials (IAM), Jiangsu National Synergetic Innovation Center for Advanced Materials (SICAM), Nanjing Tech University (NanjingTech), Nanjing 211816, P.R. China. E-mail: iamxcdong@njtech.edu.cn
[b] School of Chemical and Biomedical Engineering, Nanyang Technological University, 62 Nanyang Drive, 637459, Singapore. E-mail: chenpeng@ntu.edu.sg
[c] School of Pharmaceutical Sciences, Nanjing Tech University (NanjingTech), Nanjing 211816, P.R. China. E-mail: zhangqi@njtech.edu.cn

† Electronic Supplementary Information (ESI) available: Experimental details and supplementary figures. See DOI: 10.1039/x0xx00000x

View Article Online
DOI: 10.1039/C6TB02979E

cytotoxicity of the inorganic photosensitizers,[15] requirement for dual-wavelength laser irradiation, requirement for multiple functional components, or tedious synthesis process. In addition, the laser sources are bulky and expensive; laser may cause discomfort, erythema, crusting, blistering, and dyspigmentation;[16] and the narrow bandwidth of lasers restricts their use to specific photosensitisers only.[17] In comparison with lasers, lamps are cheap broad-band light sources that can be easily handled and maintained in clinical settings.[18] Therefore, it is highly desirable to design a biocompatible photosensitizer which can simultaneously provide PTI, PAI, PDT and PTT using a single broad-band light source.

Herein, a BF_2 Chelate of [4-iodo-5-(4-bromophenyl)-3-(4-methoxyphenyl)-1H-pyrrol-2-yl] [4-iodo-5-(4-bromophenyl)-3-(4-methoxyphenyl)pyrrol-2-ylidene]amine (IABDP) has been synthesized. Owing to the exceptional photophysical properties,[19] such as large molar absorption coefficient for visible light, high fluorescence quantum yield, narrow emission band and good photostability, aza-Bodipy was chosen as the triplet photosensitizer. Iodo-substituents as well as bromine-substituents were introduced to increase the singlet oxygen quantum yield (the synthesis routes shown in Scheme S1†). And the biocompatible and water soluble nanoparticles (NPs) self-assembled from IABDP molecules are employed as the common photosensitizer for PTI and PAI guided dual modal phototherapy (PDT and PTT) (Scheme 1). IABDP NPs can passively yet selectively target the tumor because of the enhanced permeability and retention (EPR) effect.[20] The IABDP NPs with strong absorption in the NIR region shows high singlet oxygen quantum yield, excellent photothermal conversion efficiency and outstanding photoacoustic (PA) response. Both *in vitro* and *in vivo* studies demonstrate the good biosafety and high anti-tumor efficiency of IABDP NPs under irradiation of a broad-band Xenon Lamp.

Results and discussion

Synthesis and characterization of IABDP NPs

As shown in Scheme S1 (see ESI†), water-soluble IABDP NPs were prepared through a simple self-assembly strategy with the assistance of amphiphilic 1,2-distearoyl-sn-glycero-3-phosphoethanolamine- N-[methoxy(polyethylene glycol)-2000] (DSPE- $mPEG_{2000}$). The morphology of the nanoparticles can be controlled by the ultrasonic power and the concentrations of IABDP and DSPE-$mPEG_{2000}$, ranging from spherical to cubic NPs. As revealed by transmission electron microscopy (TEM), the average size of the cubic and spherical NPs is about 150 nm (Fig. 1a) and 60 nm (Fig. S1†), respectively.

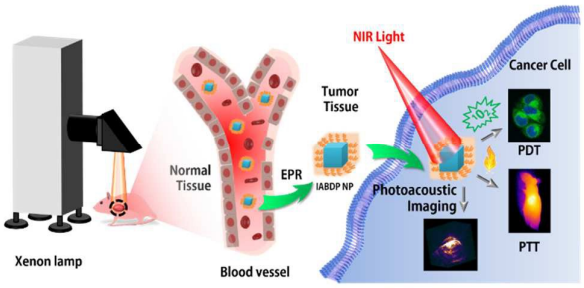

Scheme 1 Schematic illustration of PAI and PTI guided PTT/PDT synergistic phototherapy with Xenon lamp irradiation, using IABDP NPs.

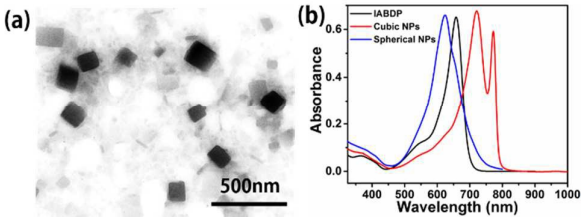

Fig. 1 (a) TEM images of cubic IABDP NPs. (b) UV/Vis absorption spectra of IABDP molecules in dichloromethane and IABDP NPs in PBS solution, respectively.

As shown in Fig. 1b, the absorption peak of the spherical IABDP NPs is observed at ~624 nm, which has a slight blue shift as compared with free IABDP molecules (at ~658 nm). In contrast, the adsorption of cubic IABDP NPs is greatly red-shifted with two prominent peaks at ~721 and 772 nm. Similar shape-dependent adsorption has also been reported by Liu et al.[21] Conceivably, this phenomenon can be attributed to the structure specific intermolecular interaction and charge transfer. Free IABDP molecules weakly fluoresce (peaking at ~714 nm upon 658 nm excitation) because of the quenching effect induced by the heavy atoms (Fig. S2†). At 624 nm excitation, the spherical IABDP NPs give two broad emission peaks at ~694 and ~733 nm and a narrower peak at ~829 nm. In comparison, the cubic NPs have two narrow emission peaks at 791 and 831 nm, under 721 nm excitation. To achieve deep tissue penetration in the NIR window, the cubic NPs were employed in the following experiments.

The singlet oxygen quantum yield of IABDP, which is the key to PDT efficiency, was assessed by monitoring oxidation-caused adsorption decrease of 1, 3-diphenylisobenzofuran (DPBF) at 414 nm in dichloromethane under 660 nm laser irradiation (Fig. S3a†). With reference to methylene blue trihydrate (0.57 in dichloromethane) as the standard,[19] IABDP demonstrates an outstanding singlet oxygen generation efficiency (~0.92, Fig. S3b†). As compared in Table S1 (see ESI†), the singlet oxygen quantum yield of IABDP is much higher than the previously reported photosensitizers. Presumably, the high singlet oxygen quantum yield is due to the two iodo-substituents attached at the π-core of Aza-BODIPY because these heavy atoms are able to greatly enhance the intersystem crossing of the excited electrons.[22] Under broadband irradiation from a Xenon lamp, IABDP NPs in the physiological solution (PBS with pH 7.4) are also able to efficiently produce singlet oxygen as evidenced by the decrease of DPBF adsorption in an irradiation duration dependent manner (Fig. 2a).

In addition to the prominent photodynamic activity, IABDP NPs also possess high photothermal conversion ability. The

View Article Online
DOI: 10.1039/C6TB02979E

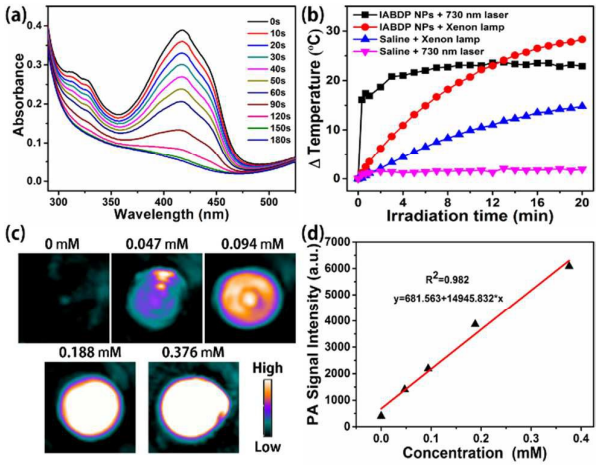

Fig. 2 (a) Absorption spectra of DPBF (ROS reporter) in the presence of IABDP NPs (94 μM) and Xenon lamp irradiation for different durations. (b) Temperature curves of saline solution or IABDP NP solution with 730 nm laser or Xenon lamp irradiation. (c) PA images of PBS solution containing IABDP NPs of different concentrations. (d) The relationship between concentration of IABDP NPs and PA signal intensity.

photothermal conversion efficiency of ~37.9% was obtained under the irradiation of 730 nm laser (Fig. S4†), which is higher than that of the previously reported photothermal agents (see comparison in Table S2†). Almost no photodegradation of IABDP NPs aqueous solution after irradiation of 730 nm laser can be observed, confirming the excellent photostability of IABDP NPs (Fig. S5†). As shown in Fig. 2b, under the irradiation of 730 nm laser, the temperature of IABDP NPs solution rapidly increased ~20 ^{o}C within a short time (~3 min). In the control experiment, the temperature of the saline solution essentially remained the same, implying the unwanted heating of biofluids can be avoided. Although the temperature increase kinetics of IABDP NP solution is slower under Xenon lamp, an increase of 28.3 ^{o}C was attained after 20 min, which is even higher than the maximum temperature increase induced by 730 nm laser (23.7 ^{o}C). In contrast, the same irradiation under Xenon lamp only caused very slow and mild temperature increase of the saline solution. These observations indicate that broadband Xenon lamp irradiation is advantageous over the commonly used laser irradiation. In addition to the PDT and PTT effects, IABDP NPs also exhibit bright photoacoustic signal in saline (Fig. 2c), which is linearly proportional to their concentration (Fig. 2d).

***In vitro* cell experiments**

To examine the synergistic phototherapeutic effects of IABDP NPs on cells *in vitro*, 3-(4,5-dimethylthiazol-2-yl)-2,5-diphenyl-tetrazolium bromide (MTT) assay was carried out. As demonstrated in Fig. 3a, the viability of the cell incubated with various concentrations of IABDP NPs significantly decreased under Xenon lamp irradiation in a dose-dependent manner with a half-maximal inhibitory concentration (IC_{50}) of ~47 μM, whereas the untreated cells have small dark toxicity with cell viability of ~80% at high concentration range (about >40 μM). Such good biocompatibility and high photo-toxicity of IABDP NPs make them desirable for selective cancer therapy.

Since the fluorescence of IABDP is largely quenching due to its heavy atoms (especially the two iodo-substituents) and the adjacent IABDP molecules tightly packed together in the nanoparticle, the cellular uptake of IABDP NPs cannot be visually confirmed by confocal microscopy. Alternatively, the abundant and homogenous uptake of IABDP NPs into HeLa cells was clearly evidenced by the strong photoacoustic (PA) signal collected from the cells pre-incubated with the nanoparticles but not those untreated cells (Fig. 3b).

Using 2',7'-dichlorofluorescin diacetate (DCFH-DA) as the probe, generation of ROS by IABDP NPs can be visualized in living cells because ROS converts non-fluorescent DCFH-DA into fluorescent 2',7'-dichlorofluorescein (DCF) after deacetylate by on lamp, strong green fluorescence distributed throughout the HeLa cells treated with IABDP NPs and DCFH-DA molecules, especially in the periphery of the nuclei (stained wiesterase.[23] Fig. 3c shows that, after illumination with a Xenth blue fluorescent 4',6-diamidino-2-phenylindole molecules, DAPI). In the control experiment, the same irradiation but without IABDP NPs did not cause any green fluorescence, indicating no ROS generation. This result certifies the ability of IABDP NPs to intracellularly generate ROS under Xenon lamp irradiation.

Dual-modal *in vivo* imaging

Photoacoustic imaging was used to monitor in real-time the dynamic accumulation and metabolism of IABDP NPs in mouse tumor (Fig. 4a). Before injection of IABDP NPs, weak PA signal from the blood vessels was observed owing to the endogenous light absorbing hemoglobin molecules in the blood. One hour later after tail intravenous injection of IABDP NPs, PA signal increased greatly (particularly near the blood vessels),

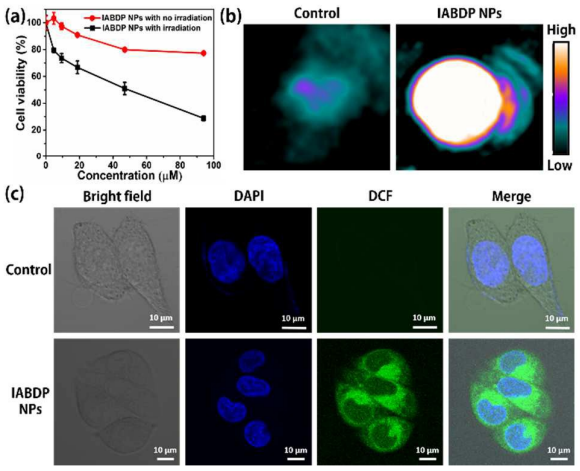

Fig. 3 (a) Cell viability reported by MTT assay of HeLa cells after treatment with different concentrations of IABDP NPs in the presence and absence of irradiation. (b) PA image of HeLa cells with or without internalized IABDP NPs. (c) Confocal images of DAPI and DCFH-DA stained HeLa cells with or without being pre-incubated with IABDP NPs.

View Article Online
DOI: 10.1039/C6TB02979E

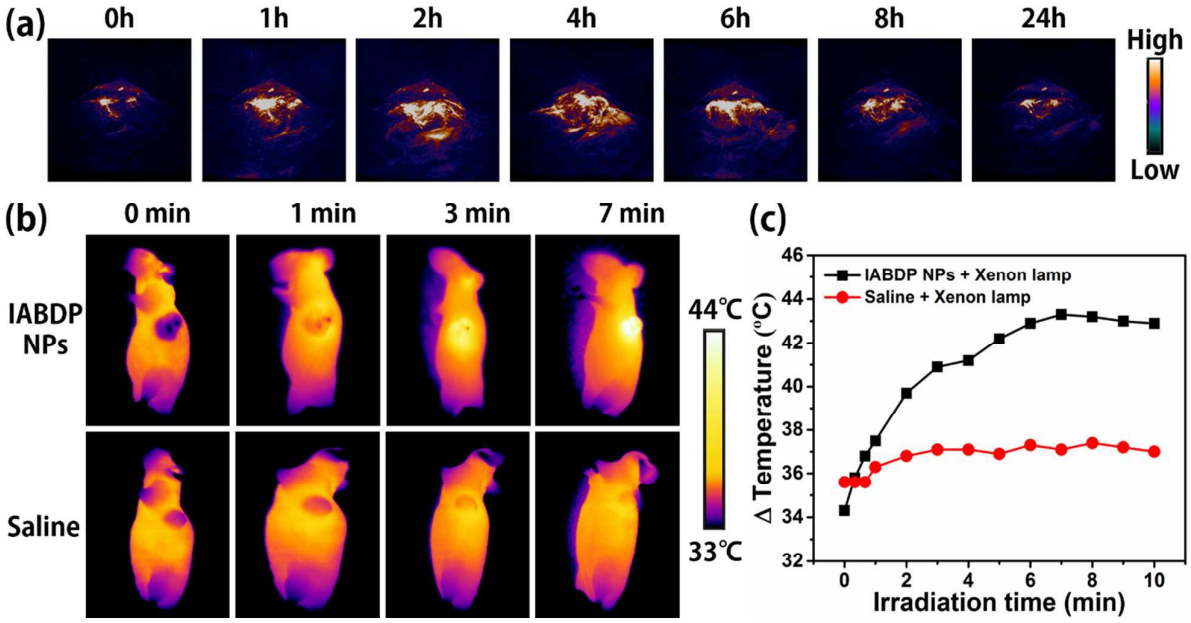

Fig. 4 (a) *In vivo* PA images of the mouse tumor taken at different time points after tail intravenous injection of IABDP NPs. (b) *In vivo* PT images of HeLa tumor-bearing nude mice after tail intravenous injection of IABDP NPs with Xenon lamp irradiation. (c) Tumor temperature curves under Xenon lamp irradiation.

indicating that IABDP NPs just entered the tumor tissue through so-called enhanced permeability and retention (EPR) effect. Over time, IABDP NPs spread throughout the tumor tissue, reaching the strongest PA intensity at 4th hour. Subsequently, PA signal started to decrease, suggesting that IABDP NPs were metabolized. As shown by PA imaging, IABDP NPs are able to preferentially target on tumors. It implies that the size of IABDP NPs is especially suitable for their penetration through the defective blood vessels and subsequent retention in tumor tissue. Furthermore, PAI assists to accurately locate and irradiate the tumor site but not the surrounding normal tissues.

Notably, IABDP NPs have excellent photothermal conversion ability even under irradiation of Xenon lamp. Fig. 4b shows the PT images of the tumor site at various time points during the continuous irradiation of Xenon lamp, confirming the tumor accumulation of IABDP NPs and revealing the photothermal conversion kinetics. For those mice with IABDP NPs injection, the tumor temperature gradually escalated to ~43 °C within 10 min (Fig. 4b and c), which is high enough to eliminate tumor cells but not too high to cause unwanted tissue damages.[24] Noteworthy, the cell membrane permeability increases at such moderately high temperature (43-45 °C), and consequently, the cellular uptake of the nanoparticles (hence the effectiveness of phototherapy) is enhanced.[25] Additionally, the mild hyperthermia promotes blood circulation into the tumor and thus alleviates the hypoxia condition in the tumor microenvironment,[26] which is greatly helpful for improving PDT efficacy. On the contrary, the tumor temperature of the mice with saline injection showed no appreciable change under Xeon lamp irradiation (Fig. 4b and c). Taken together, both PAI and PTI provide important guidance for phototherapy and demonstrate the unique capability of IABDP NPs as the common and effective photosensitizer for *in vivo* dual modal phototherapy.

***In vivo* synergistic phototherapy**

View Article Online
DOI: 10.1039/C6TB02979E

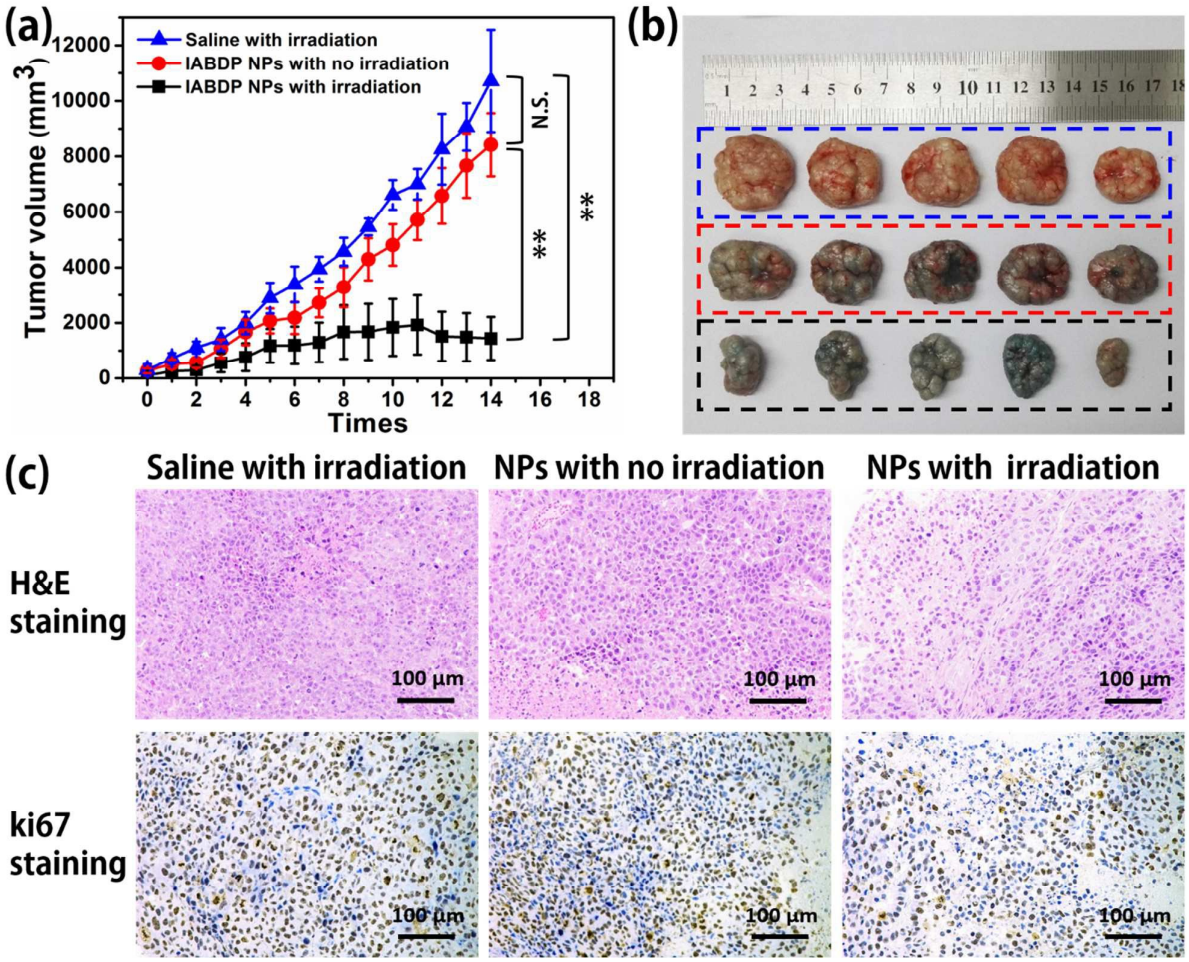

Fig. 5 (a) Tumor growth curves of 3 differently treated mouse groups (5 mice per group). Error bars represent the standard deviations (no significance or N.S, **p < 0.01). (b) Photographs of tumors collected from the mice treated with saline injection and irradiation (top), the mice treated with IABDP NP injection but without irradiation (middle), or the mice treated with both IABDP NP injection and irradiation (bottom), respectively. (c) H&E staining and Ki67 immuno-staining of tumor tissues after different treatments.

To examine the PDT and PTT synergistic therapeutic effects of IABDP NPs *in vivo*, HeLa tumor-bearing nude mice with initial tumor volumes of 100-300 mm^3 were randomly divided into 3 groups (5 mice/group): (i) the treatment group with tail intravenous injection of IABDP NPs and broadband irradiation by a Xeon lamp. (ii) the comparison group with nanoparticle injection but not irradiation. (iii) the control group with injection of saline solution and lamp irradiation. As demonstrated in Fig. 5a and b, the tumor volume steadily expanded over time (28 days) for both control and comparison groups and no significant difference was noticed between the two groups. In contrast, 14 times of phototherapy treatments during the course greatly inhibited the tumor growth (87.2% inhibition as compared to the control group). This is superior to the previously reported methods based on single phototherapy mode (PDT or PTT),[27] testifying the advantage of synergistic therapy. All the mice were sacrificed after *in vivo* experiments and their tumor tissues were collected for further investigation. The photographs of these tumors corroborate the outstanding efficacy of the phototherapy and the similarly darker color for both comparison and treatment groups also confirms the accumulation of IABDP NPs in tumor. The difference of tumor weight between the 3 groups (Fig. S6†) is consistent with the observed volume change (Fig. 5a). The obvious body weight gain of the mice in the comparison group implies that the injected IABDP NPs are non-toxic without photo irradiation, while the slight body weight increase of both control and treatment groups suggests the good tolerance of the phototherapy and insignificance of photo-induced side effects (Fig. S7†).

To further understand the therapeutic effects down to the cellular level, hematoxylin and eosin (H&E) staining as well as Ki67 immuno-staining were employed to reveal the morphology and proliferation of the tumor cells. As shown in Fig. 5c, the H&E staining indicates that the tumor cells of the control group are plump and arranged closely with the nuclei

View Article Online
DOI: 10.1039/C6TB02979E

in good condition. Only a small fraction of the tumor cells in the comparison group appear damaged by the nanoparticles. In the stark contrast, the tumor cells of the treated group shrink largely, leaving large gaps between adjacent cells. Such high level of necrosis and apoptosis evidences the effectiveness of phototherapy with IABDP NPs. The Ki67 immuno-staining assay shows that Ki67 proteins (cellular marker for proliferation) expressed at low level in the treatment group and high level in the control group, indicating IABDP NP's ability to potently inhibit the proliferation of tumor cells. Fig. S8 (in ESI†) presents the H&E staining of the major organs (heart, lung, liver, spleen, and kidney). Compared with the control group, no obvious histological alterations can be identified for the other two groups injected with IABDP NPs, further confirming the *in vivo* biocompatibility of our nanoparticles. The main text of the article should appear here with headings as appropriate.

Experimental Section

Preparation of cubic IABDP NPs. IABDP (2.0 mg) in 2 mL THF was swiftly dropped into DSPE-mPEG_{2000} aqueous solution (20.0 mg, 10 mL H_2O) under sonication (250 W). THF was then removed under reduced pressure. A royal blue aqueous solution was obtained. The aqueous solution was further filtered through 0.45 μm filter and washed with deionized water, which was freeze-dried to obtain royal blue cubic NPs powder.

Preparation of sphere IABDP NPs. IABDP (1.0 mg) in 2 mL THF was swiftly dropped into DSPE-mPEG_{2000} aqueous solution (10.0 mg, 10 mL H_2O) under sonication (175 W). THF was then removed under reduced pressure. A royal blue aqueous solution was obtained. The aqueous solution was further filtered through 0.45 μm filter and washed with deionized water, which was freeze-dried to give sphere as royal blue powder.

Singlet oxygen detection of IABDP NPs. The singlet oxygen generation of IABDP NPs was detected with DPBF as $^1O_2$ fluorescent probe in PBS solution at pH 7.4. Briefly, 20 μM DPBF was added to IABDP NPs solution with the absorbance around 0.2-0.3. Then the mixture was irradiated with a Xenon lamp (> 600 nm, 20 mW cm^{-2}) for 180 s. The oxidation of DPBF (at 418 nm) *vs.* irradiation time was monitored by UV-VIS-NIR spectrophotometer.

Cell culture. The human cervical cancer HeLa cell line used in this study was provided by the Institute of Biochemistry and Cell Biology, SIBS, CAS (China). HeLa cells were cultured in Dulbecco's Modified Eagle Medium (DMEM High Glucose, Gibco) supplemented with 1% (v/v) antibiotics (penicillin and streptomycin, GENMED) and 10% (v/v) fetal bovine serum (FBS) at 37 °C under humidified atmosphere of 5% CO_2.

MTT assays. To study the toxicity of IABDP NPs, HeLa cells were seeded into two 96-well plates at a density of 5000 cells per well and incubated in the culture media (200 μL) at 37 °C under 5% CO_2 atmosphere for 24 h, and further incubation with various concentrations (4.7, 9.4, 18.8, 47, 94 μM) of IABDP NPs in DMEM media (200 μL/well) for another 24 h in dark. After removing the culture media including IABDP NPs, these two 96-well plates were washed with phosphate buffered saline (PBS) solution and added 200 μL fresh culture medium. Then one of these 96 well plates was irradiated under a Xenon lamp (> 600 nm, 20 mW cm^{-2}) at room temperature for 10 min. After illumination, these 96-well plates were incubated for additional 12 h at 37 °C. Finally, MTT solution in PBS (3-(4,5-dimethyl-2-thiazolyl)-2,5-diphenyl-2-H-tetrazolium bromide, 5 mg mL^{-1} , 20 μL) was added to each well and incubated for 4 h. After removing the medium, 150 μL of DMSO was added into each well to dissolve formazan, and the absorbance was measured at 490 nm using an enzyme-labeled instrument. The cell viability values were calculated by the following formula:

Cell viability (%) = (mean of absorbance value of treatment group)/(mean of absorbance value of control group) ×100.

ROS detection *in vitro*. HeLa cells were seeded into a glass bottom Petri dish and incubated in the culture media (2 mL) at 37 °C under 5% CO_2 for 24 h, followed by incubation in media containing IABDP NPs (50 μM, 2 mL) for additional 24 h. In the control group, cells were just incubated in the culture media without IABDP NPs. After removing these media, the cells were washed thrice with PBS solution, and further incubated with DCFH-DA for 20 min and DAPI for 3 min in darkness, respectively. Then the cells were rinsed thrice with PBS solution and illuminated upon a Xenon lamp (> 600 nm, 20 mW cm^{-2}) for 10 min. After that, the fluorescence images of the cells were obtained using a confocal laser scanning microscopy (Olympus IX 70 inverted microscope). For DCF detection, 488 nm laser was used for excitation, and the fluorescence from 500 nm to 600 nm was collected. For DAPI detection, 405 nm laser was used for excitation, and the fluorescence from 420 nm to 500 nm was collected.

Animals and tumor model. Female athymic nude mice (4-week old, about 20 g, Permit number: SCXK(Su)2012-0004) used in this study were bought from Comparative Medicine Centre of Yangzhou University. All animal experiments conformed to the NIH guidelines for the care and use of laboratory animals are approved by School of Pharmaceutical Science, Nanjing Tech University. The subcutaneous xenograft model of cervical cancer was built by injecting 3×10^6 HeLa cells in 100 μL PBS solution subcutaneously into the left flank near the front armpit of the mice. After the tumor volumes were about 100-300 mm^3, mice were employed randomly in dual-modal imaging and phototherapy.

***In vivo* imaging.** 100 μL IABDP NPs solution (0.5 mM) in saline was given into HeLa tumor-bearing nude mice through tail intravenous injection. At different time points after tail intravenous injection of IABDP NPs, *in vivo* PA images were conducted using the Endra Nexus128 small animal photoacoustic imaging system at 721 nm. The temperature was also monitored through a FLIR thermal camera under irradiation of Xenon lamp (20 mW cm^{-2}) for 10 min at 4 hours post-injection. The mice injected with saline were evaluated as control.

***In vivo* synergistic therapy.** Nude mice bearing HeLa tumor were randomly divided into 3 groups (5 mice per group). 4 h

View Article Online
DOI: 10.1039/C6TB02979E

after injection, the control group and the treatment group were irradiated with a Xenon lamp (20 mW cm-2) for 10 min. The body weights and tumor sizes of mice were monitored every two days and tumor volumes were computed by the equation: volume = length×width^2/2. The inhibition rate was computed by the equation:

Inhibition rate (%) =100-(mean of final tumor volumes of treatment group-mean of initial tumor volumes of treatment group)/(mean of final tumor volumes of control group-mean of initial tumor volumes of control group) ×100.

All mice were sacrificed after 14 times of treatment. Tumors and the major organs (heart, lung, liver, spleen, and kidney) of three groups were fixed in 10% formalin and embedded in paraffin wax for further histomorphological analysis.

Histological examination and immunohistochemical analysis. The hematoxylin and eosin (H&E) staining and Ki67 immunostaining assays were carried out to stain tissue slices. Both the tumor tissues and the major organs (heart, lung, liver, spleen, and kidney) were stained with H&E for histological examination. Additionally, the tumor tissues were stained with anti-human Ki-67 to reflect the proliferation of tumor cells.

Conclusions

In summary, a novel aza-bodipy photosensitizer (IABDP) with high yield of singlet oxygen and excellent photothermal conversion efficiency has been successfully designed and synthesized. We demonstrate that the NIR absorbing IABDP nanoparticles (NPs) are able to serve as the common agent for photoacoustic (PA) and photothermal (PT) imaging guided photothermal/photodynamic therapy under broadband irradiation by a Xeon lamp. The simplicity of this platform is highly desirable for the convenient and reproducible practical use. The synergistic dual modal phototherapy renders the high efficacy of the method. The dual modal imaging enables accurate localization of tumor site in order to avoid unwanted tissue damages, real-time monitoring of the photosensitizer distribution and its accumulation/metabolism kinetics, and real-time monitoring of temperature change at the tumor site in order to determine the optimal irradiation protocol. In comparison to inorganic nanomaterial based photosensizers, IABDP NPs can rapidly and selectively target to the tumor site and can be readily metabolized instead of being retained for too long. Both *in vitro* and *in vivo* studies demonstrate the negligible dark toxicity yet remarkable phototoxicity of IABDP NPs. The *in vivo* experiments show that these nanoparticles can potently inhibit tumor growth without causing noticeable side-effects.

Acknowledgements

The work was supported by NNSF of China (61525402, 21275076), Key University Science Research Project of Jiangsu Province (15KJA430006), QingLan Project.

Notes and references

1 (a) J. Tian, L. Ding, H. Ju, Y. Yang, X. Li, Z. Shen, Z. Zhu, J.S. Yu, C.J. Yang, *Angew. Chem. Int. Ed. Engl*., 2014, **53**, 9544-9549; (b) J. Mou, T. Lin, F. Huang, H. Chen, J. Shi, *Biomaterials*, 2016, **84**, 13-24; (c) J. Cao, H. An, X. Huang, G. Fu, R. Zhuang, L. Zhu, J. Xie, F. Zhang, *Nanoscale*, 2016, **8**, 10152-10159; (d) J. Han, H. Xia, Y. Wu, S.N. Kong, A. Deivasigamani, R. Xu, K.M. Hui, Y. Kang, *Nanoscale*, 2016, **8**, 7861-7865; (e) G. Wang, F. Zhang, R. Tian, L. Zhang, G. Fu, L. Yang, L. Zhu, *Acs Appl. Mater. Interfaces*, 2016, **8**, 5608-5617; (f) Y. Cai, Q. Tang, X. Wu, W. Si, Q. Zhang, W. Huang, X. Dong, *Acs Appl. Mater. Interfaces*, 2016, **8**, 10737-10742.

2 (a) Y. Liu, Y. Liu, W. Bu, C. Cheng, C. Zuo, Q. Xiao, Y. Sun, D. Ni, C. Zhang, J. Liu, J. Shi, *Angew. Chem. Int. Ed. Engl.* , 2015, **54**, 8105-8109; (b) H. Wu, F. Zeng, H. Zhang, J. Xu, J. Qiu, S. Wu, *Adv. Sci.*, 2016, **3**, 1500254.

3 (a) C.S. Jin, J.F. Lovell, J. Chen, G. Zheng, *Acs Nano*, 2013, **7**, 2541-2550; (b) C. Zhang, K. Zhao, W. Bu, D. Ni, Y. Liu, J. Feng, J. Shi, *Angew. Chem. Int. Ed. Engl.*, 2015, **54**, 1770-1774.

4 K. Deng, Z. Hou, X. Deng, P. Yang, C. Li, J. Lin, *Adv. Funct. Mater.*, 2015, **25**, 7280-7290.

5 L. Li, C. Chen, H. Liu, C. Fu, L. Tan, S. Wang, S. Fu, X. Liu, X. Meng, H. Liu, *Adv. Funct. Mater.,* 2016, DOI: 10.1002/adfm.201600985.

6 D. Luo, K.A. Carter, D. Miranda, J.F. Lovell, *Adv. Sci.,* 2016, DOI: 10.1002/advs.201600106.

7 X. Song, H. Gong, S. Yin, L. Cheng, C. Wang, Z. Li, Y. Li, X. Wang, G. Liu, Z. Liu, *Adv. Funct. Mater.,* 2014, **24**, 1194-1201.

8 G. Song, Q. Wang, Y. Wang, G. Lv, C. Li, R. Zou, Z. Chen, Z. Qin, K. Huo, R. Hu, J. Hu, *Adv. Funct. Mater.,* 2013, **23**, 4281-4292.

9 F. He, G. Yang, P. Yang, Y. Yu, R. Lv, C. Li, Y. Dai, S. Gai, J. Lin, *Adv. Funct. Mater.,* 2015, **25**, 3966-3976.

10 L.V. Wang, S. Hu, *Science*, 2012, **335**, 1458-1462.

11 (a) M. Yu, F. Guo, J. Wang, F. Tan, N. Li, *Biomaterials*, 2016, **79**, 25-35; (b) U.S. Chung, J.-H. Kim, B. Kim, E. Kim, W.-D. Jang, W.-G. Koh, *Chem. Commun.*, 2016, **52**, 1258-1261; (c) C.-K. Chu, Y.-C. Tu, J.-H. Hsiao, J.-H. Yu, C.-K. Yu, S.-Y. Chen, P.-H. Tseng, S. Chen, Y.-W. Kiang, C.C. Yang, *Nanotechnology,* 2016, **27**, 115102; (d) G.-F. Luo, W.-H. Chen, Q. Lei, W.-X. Qiu, Y.-X. Liu, Y.-J. Cheng, X.-Z. Zhang, *Adv. Funct. Mater.,* 2016, DOI: 10.1002/adfm.201505175.

12 (a) I. Marangon, C. Menard-Moyon, A.K.A. Silva, A. Bianco, N. Luciani, F. Gazeau, *Carbon*, 2016, **97**, 110-123; (b) H. Zhang, X. Jiao, Q. Chen, Y. Ji, X. Zhang, X. Zhu, Z. Zhang, *Nanotechnology,* 2016, **27**, 085104; (c) B.-P. Jiang, L.-F. Hu, X.-C. Shen, S.-C. Ji, Z. Shi, C.-J. Liu, L. Zhang, H. Liang, *Acs Appl. Mater. Interfaces*, 2014, **6**, 18008-18017; (d) P. Zhang, H. Huang, J. Huang, H. Chen, J. Wang, K. Qiu, D. Zhao, L. Ji, H. Chao, *Acs Appl. Mater. Interfaces*, 2015, **7**, 23278-23290.

13 J. Qiu, Q. Xiao, X. Zheng, L. Zhang, H. Xing, D. Ni, Y. Liu, S. Zhang, Q. Ren, Y. Hua, K. Zhao, W. Bu, *Nano Res.*, 2015, **8**, 3580-3590.

14 (a) Y. Yong, L. Zhou, Z. Gu, L. Yan, G. Tian, X. Zheng, X. Liu, X. Zhang, J. Shi, W. Cong, W. Yin, Y. Zhao, *Nanoscale*, 2014, **6**, 10394-10403; (b) H. Bi, Y. Dai, R. Lv, C. Zhong, F. He, S. Gai, A. Gulzar, G. Yang, P. Yang, *Dalton Trans.*, 2016, **45**, 5101-5110; (c) C. Wu, A. Zhu, D. Li, L. Wang, H. Yang, H. Zeng, Y. Liu, *Expert Opin. Drug Del.*, 2016, **13**, 155-165; (d) J. Hao, G. Song, T. Liu, X. Yi, K. Yang, L. Cheng, Z. Liu, *Adv. Sci.,* 2016, DOI: 10.1002/advs.201600160; (e) Y. Chen, L. Wang, J. Shi, *Nano Today,* 2016, **11**, 292-308; (f) S. Wang, Y. Chen, X. Li, W. Gao, L. Zhang, J. Liu, Y. Zheng, H. Chen, J. Shi, *Adv. Mater.,* 2015, **27**, 7117-7122.

15 (a) H. Gong, Z. Dong, Y. Liu, S. Yin, L. Cheng, W. Xi, J. Xiang, K. Liu, Y. Li, Z. Liu, *Adv. Funct. Mater.* 2014, **24**, 6492-6502; (b) E.B. Ehlerding, F. Chen, W. Cai, *Adv. Sci.,* 2016, **3**, 1500223.

View Article Online
DOI: 10.1039/C6TB02979E

16 M. Alexiades-Armenakas, *Clin. Dermatol.*, 2006, **24**, 16-25.
17 B. Javaid, P. Watt, N. Krasner, *Laser. Med. Sci.*, 2002, **17**, 51-56.
18 L. Brancaleon, H. Moseley, *Laser. Med. Sci.*, 2002, **17**, 173-186.
19 S. Guo, L. Ma, J. Zhao, B. Kucukoz, A. Karatay, M. Hayvali, H.G. Yaglioglu, A. Elmali, *Chem. Sci.*, 2014, **5**, 489-500.
20 (a) M. Zhen, C. Shu, J. Li, G. Zhang, T. Wang, Y. Luo, T. Zou, R. Deng, F. Fang, H. Lei, C. Wang, C. Bai, *Science China Materials,* 2015, **58**, 799-810; (b) Y. Li, *Science China Materials,* 2015, **58**, 851-851; (c) H. Maeda, J. Wu, T. Sawa, Y. Matsumura, K. Hori, *J. Control. Release*, 2000, **65**, 271-284.
21 D. Liu, C. Li, F. Zhou, T. Zhang, H. Zhang, X. Li, G. Duan, W. Cai, Y. Li, *Sci. Rep.*, 2015, **5**, 7686.
22 A. Gorman, J. Killoran, C. O'Shea, T. Kenna, W.M. Gallagher, D.F. O'Shea, *J. Am. Chem. Soc.*, 2004, **126**, 10619-10631.
23 (a) K. Han, W.-Y. Zhang, J. Zhang, Q. Lei, S.-B. Wang, J.-W. Liu, X.-Z. Zhang, H.-Y. Han, *Adv. Funct. Mater.,* 2016, DOI: 10.1002/adfm.201600170; (b) K. Han, Q. Lei, S.-B. Wang, J.-J. Hu, W.-X. Qiu, J.-Y. Zhu, W.-N. Yin, X. Luo, X.-Z. Zhang, *Adv. Funct. Mater.*, 2015, **25**, 2961-2971; (c) H. Shi, W. Sun, C. Liu, G. Gu, B. Ma, W. Si, N. Fu, Q. Zhang, W. Huang, X. Dong, *J. Mater. Chem. B*, 2016, **4**, 113-120; (d) X. Zhou, H. Liang, P. Jiang, K.Y. Zhang, S. Liu, T. Yang, Q. Zhao, L. Yang, W. Lv, Q. Yu, W. Huang, *Adv. Sci.* 2016, **3**, 1500155; (e) Y. Cai, Q. Tang, X. Wu, W. Si, W. Huang, Q. Zhang, X. Dong, *ChemistrySelect*, 2016, **1**, 3071-3074.
24 A. Gulzar, S. Gai, P. Yang, C. Li, M.B. Ansari, J. Lin, *J. Mater. Chem. B*, 2015, **3**, 8599-8622.
25 (a) T. Liu, C. Wang, W. Cui, H. Gong, C. Liang, X. Shi, Z. Li, B. Sun, Z. Liu, *Nanoscale*, 2014, **6**, 11219-11225; (b) S.P. Sherlock, S.M. Tabakman, L. Xie, H. Dai, *Acs Nano*, 2011, **5**, 1505-1512.
26 X. Yi, K. Yang, C. Liang, X. Zhong, P. Ning, G. Song, D. Wang, C. Ge, C. Chen, Z. Chai, Z. Liu, *Adv. Funct. Mater.*, 2015, **25**, 4689-4699.
27 (a) Y. Li, J. Tang, D.-X. Pan, L.-D. Sun, C. Chen, Y. Liu, Y.-F. Wang, S. Shi, C.-H. Yan, *Acs Nano*, 2016, **10**, 2766-2773; (b) Z. L. Li, Y. Hu, K. A. Howard, T. T. Jiang, X. L. Fan, Z. H. Miao, Y. Sun, F. Besenbacher, M. Yu, *Acs Nano*, 2016, **10**, 984-997.

View Article Online
DOI: 10.1039/C6TB02979E

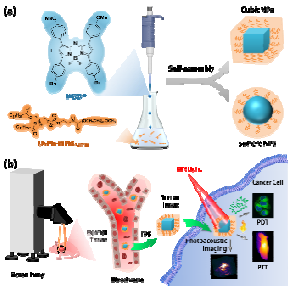

A novel NIR absorbing aza-bodipy photosensitizer with high $^1O_2$ quantum yield and excellent photothermal conversion efficiency were designed for synergistic phototherapy.